Compact Single-Layer mm-Wave Planar Antenna with Suppressed Surface-Wave Excitation

Louis Delait, Christophe Craeye, *Senior Member, IEEE*, Zhenming Tian, Shiqi Ma, Andreas Rennings, *Member, IEEE*, Jean-Pierre Raskin, *Fellow, IEEE* and Dimitri Lederer, *Member, IEEE*

***Abstract*—A new millimeter-wave planar antenna concept is introduced that minimizes the excitation of surface-wave power in the substrate. The proposed antenna uses a single metal layer and does not rely on additional fabrication steps or auxiliary structures such as vias, substrate etching, superstrates, dielectric resonators, or lenses, making it compatible with most manufacturing processes, either on-chip or in-package. The design is based on the principle, introduced in this paper for the first time, that a ring of electric current in a multilayer grounded stack does not excite the dominant TM_0 surface-wave when its radius is properly selected. From the Green's function analysis in the Fourier domain, the design rule for such a ring is derived as a tool for antenna designers. The concept is experimentally demonstrated at W-band (75-110 GHz) using two single-metal-layer prototypes fabricated on high-resistivity silicon and quartz substrates. Series capacitive loading is employed to approximate the required ring-current distribution while maintaining a compact footprint. The antennas performances are analyzed though full-wave simulations and on-wafer measurements while a reduced substrate coupling is experimentally demonstrated by 2-ports measurements on-wafer. The antennas occupy areas smaller than $\lambda_0^2/4$ on silicon and $\lambda_0^2/2$ on quartz, providing a compact and fabrication-compatible means of controlling the dominant surface-wave mode in single-layer millimeter-wave antennas.**

***Index Terms*—Antenna in-package, antenna theory and design, layered-media Green's functions, millimeter-wave and terahertz components, on-chip antenna, passive component modeling, reduced surface-wave antenna, substrate modes, surface-waves.**

I. Introduction

THE demand for mm-Wave and Sub-THz antennas has emerged across various applications, including high-resolution radar imaging [1], precise material characterization [2], and high-data-rate communication [3].

To meet the stringent requirements on integration, cost, and form factor, antennas are increasingly co-integrated with the radio-frequency integrated circuit (RFIC) front-end, either directly on the silicon die as Antennas-on-Chip (AoC) or within the package as Antennas-in-Package (AiP). AoC solutions provide the highest level of integration, enabling short interconnects, reduced parasitic effects, and compact transceivers. Although some modern processes offer low-loss substrates at mm-Wave frequencies (e.g., HR-SOI [4], [5], GaN on HR-Si [6], InP [7], [8]), AoC designs remain expensive due to the high manufacturing cost per unit area associated with semiconductor processes. AiP approaches embed the antenna within a package substrate, allowing the use of lower-permittivity dielectrics (e.g., glass, quartz, LTCC) and a reduced cost per unit area, at the expense of increased packaging complexity and interconnection losses between the antenna and the RFIC [9]–[12]. Both AoC and AiP configurations are illustrated in Figs. 1(a) and (b), where a silicon (Si) chip and quartz interposer are considered, respectively. In this example, the chip containing the RFIC front-end is connected to the quartz interposer via flip-chip, although other interconnection schemes are possible. Due to process constraints, substrates in classical AoC and AiP technologies are typically electrically thick at mm-Wave frequencies (i.e., thicker than $\lambda_m/4$ at 100 GHz, where λ_m is the wavelength in the substrate). Anten-

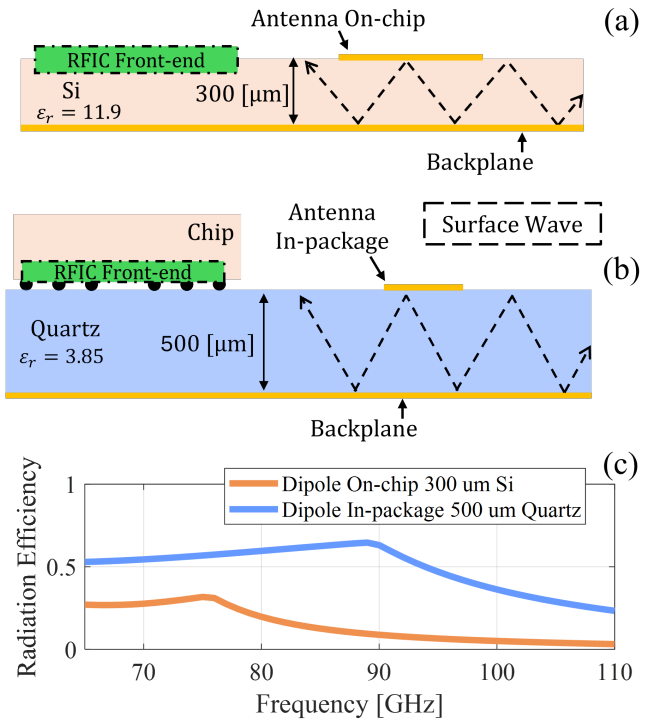


Fig. 1. (a) Reference Si semiconductor stack for antenna on-chip. (b) Reference quartz interposer stack for antenna in-package.(c) Simulated radiation efficiency of lossless canonical dipoles on Si chip and quartz interposer.

This paragraph of the first footnote will contain the date on which you submitted your paper for review.

Louis Delait, Christophe Craeye, Shiqi Ma, Jean-Pierre Raskin and Dimitri Lederer are with the Institute of Information and Communication Technologies, Electronics and Applied Mathematics (ICTEAM), Université catholique de Louvain, 1348 Ottignies-Louvain-la-Neuve, Belgium (e-mail: louis.delait@uclouvain.be).

Zhenming Tian and Andreas Rennings are with the General and Theoretical Electrical Engineering (ATE), University of Duisburg-Essen (UDE), and Center for Nanointegration Duisburg-Essen (CENIDE), D-47048 Duisburg, Germany.

nas placed on such substrates can couple a significant portion of their power to surface-waves (SWs), also known as substrate modes [13], [14]. These SWs can diffract at substrate edges, causing radiation pattern distortions and severely degrading antenna performance if not properly controlled [15]–[17]. This effect is illustrated in Fig. 1(c), which shows the simulated radiation efficiency of lossless $\lambda/2$ dipoles resonating at 85 GHz, as a function of frequency, for the AoC and AiP case scenarios on Si and quartz substrates previously described. As the simulation assumes lossless materials, all the power loss is due to the excitation of surface-waves. It is observed that, at the design frequency, the antenna on 300-µm thick Si substrate couples more than 80% of its power to SW while more than 40% of the power is coupled to SW in the case of the quartz substrate, the lower value being due to the electrically thinner substrate in this case. A metal backplane is placed beneath the substrates, as commonly encountered in practical casings, in order to suppress backside radiation and minimize coupling with underlying system components. Perfect electric conductor (PEC) models are assumed for both the backplanes and dipoles. Simulations are performed using a Method of Moments (MoM) solver in Keysight ADS [18]. Lossless materials are assumed in Fig. 1 so that the reported efficiency loss is due solely to surface-wave excitation. Metal and substrate losses are analyzed separately in Section V-A.

Several process-based solutions have been proposed to address the SW coupling of AoCs and AiPs, such as creating a resonant cavity with through-substrate vias (TSV) [7], [19], [20], local backside etching (LBE) of the substrate underneath the antenna [21], [22] and/or using artificial dielectric layers (ADL), superstrates, dielectric resonators (DR), lenses [22]–[27] atop the antenna or external radiators [28]. However, the above-mentioned techniques all require additional processing steps or the addition of auxiliary radiating elements, which add to the system cost. In particular, lenses, that are a common solution at mm-Wave and Sub-THz frequencies, are sensitive to misalignment of a few micrometers at these frequencies. Big lenses, up to several centimeters of diameter, can be used to mitigate this sensitivity, making it a bulky solution not compatible with low-profile constraints [25], [26]. There also exist solutions that do not require a complexified process flow. One can cite electromagnetic bandgap (EBG) structures [29], [30] and Metasurfaces (MTS) [10], [11] surrounding the antenna to respectively act as a resonant cavity or to convert the SW into a leaky wave mode that will participate to radiation. However, these approaches occupy a large area, which may be unavailable or prohibitively expensive. Planar EBGs usually require areas larger than λ_0^2 [29], [30], and MTSs more than $10\lambda_0^2$ [10], [11], with λ_0 the free space wavelength in vacuum.

Another option that has been investigated in [15], [31], is to design a dipole array with element spacing $\lambda_{SW}/2$, λ_{SW} being the wavelength of the considered SW mode. In this configuration, the SW excited by one element is in phase opposition with the SW generated by its neighbor. This solution, while requiring a limited area around $\lambda_0^2/4$, only leads to a partial cancellation of the excited SW, which has not been quantified. When several metal layers are available atop the substrate, a widely used strategy to avoid SW is to shield the antenna from the substrate with one or more stacked metal layers [32]–[34]. This, however, is not compatible with single layer designs and results in reduced bandwidth (BW) and efficiency as the distance from the antenna to the reflector becomes much smaller than the wavelength (i.e. smaller than $\lambda_m/100$ at 100 GHz with λ_m the free space wavelength in the substrate material). Furthermore, this solution does not take advantage of the low-loss substrate underneath the shield if available.

This paper proposes a new reduced surface-wave (RSW) antenna design approach compatible with both AoC and AiP manufacturing flows. Specifically, a novel design rule for planar antennas with suppressed SW excitation is derived from an original analytical formulation based on the imposed current distribution. The proposed solution relies on a single metal layer and does not require additional fabrication steps or auxiliary radiating elements, while remaining compact and low-profile.

The remainder of this paper is organized as follows. Section II reviews the state-of-the-art RSW antenna solutions at lower frequencies, along with their limitations for on-chip and in-package implementation. Section III then develops the analytical framework to extract the excited SW power of a planar antenna with a prior knowledge on the electrical current distribution and material stack. From that expression, the new design rule for a single layer antenna that does not excite SWs is derived in Section IV as a tool for future antenna designs. In Section V, two W-band (75–110 GHz) prototypes are proposed, based on this design rule, as on-chip and in-package demonstrators, and are analyzed through full-wave simulation and on-wafer measurement in Section IV.

II. Reduced Surface-Waves Antennas at Lower Frequencies

Several publications have proposed antenna designs that reduce or totally cancel SW excitation at lower frequency, referenced as RSW antennas.

In [35], Jackson proposed a variation of a circular microstrip patch design which does not excite SW power. The design is based on the principle that a ring of magnetic current, which models the patch, on a substrate does not excite the dominant TM_0 SW if the radius of the ring is a particular value R that is a solution of the following equation:

$$J_1'(\beta_{TM0}R) = 0, \tag{1}$$

with β_{TM0} the propagation constant of the TM_0 SW mode and $J_1'(x)$ the derivative of the Bessel function of first kind and order 1. Many RSW antennas based on this concept have been proposed since then and are summarized in [36]. This design comprises vias to make the antenna resonant at the dimension imposed by the design rule given in (1), making it not compatible with the vialess manufacturing processes targeted in this work.

In [37], the same design rule is implemented using twin arc-slots, based on the equivalence between slots and magnetic current. This design, however, does not entirely cancel the SW as the dipole-slot lengths are chosen to be resonant, and a full

ring of magnetic current cannot be implemented contrary to Jackson's design. Furthermore, for the equivalence between magnetic current and slot in a metal plane to be valid, the dimensions of the metal plane should be sufficiently large (i.e., in the order of a few wavelengths [38]). This results in very large antennas, not suitable for all on-chip or in-package implementation, as a large metal plane would be needed. Furthermore, this design is intended to radiate through the substrate and is therefore not compatible with grounded substrates, as considered in this work.

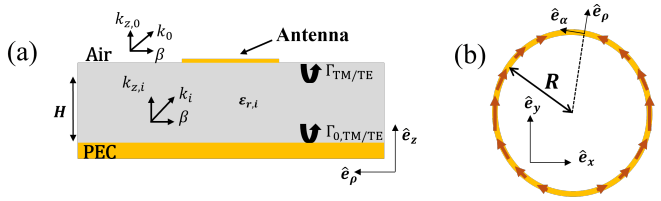


Fig. 2. (a) Multilayer stack illustration. (b) Electrical ring current distribution.

The previously reported RSW solutions rely on a magnetic current distribution which, for the reference AoC and AiP substrate stacks shown in Figs. 1(a) and (b), results in low radiated power in the W-band and, consequently, poor radiation efficiency. This behavior originates from the substrate thickness being on the order of $\lambda/4$. At the source location, the magnetic field associated with the wave reflected by the PEC backplane therefore arrives in phase opposition with respect to the upward-propagating wave, since the image of a magnetic current with respect to a PEC has the same orientation.
The radiated power from a magnetic current source M is given by:

$$P_{\text{rad},M} = \Re\left\{\frac{-1}{8\pi^2}\iint_0^{k_0} \tilde{\boldsymbol{H}}^* \cdot \tilde{\boldsymbol{M}}\, dk_x\, dk_y\right\}, \tag{2}$$

with M the magnetic current source density and H the H-field due to this current. Both quantities are expressed in the spatial Fourier domain. In this configuration, low value of H induces a low radiated power. It should be noted that, in this document, the tildes refer to quantities in the spectral domain, and the overbar in the space domain. Furthermore, bold symbols refer to vectors or tensors.

Based on these observations, this paper proposes a new RSW antenna solution that relies on the same current function introduced by Jackson in [35], but implemented through an electric current distribution, and not magnetic. This approach is well suited for antenna integration on the reference chip and package stacks shown in Figs. 1(a) and (b) in the W-band. Indeed, following a reasoning analogous to that for magnetic current sources, when the substrate thickness is on the order of $\lambda/4$, the electric field associated with the wave reflected by the PEC backplane arrives in phase with the upward-propagating wave at the source location. This behavior arises because the image of an electric current with respect to a PEC has opposite orientation.
The radiated power from an electric current source J is given by:

$$P_{\text{rad},J} = \Re\left\{\frac{-1}{8\pi^2}\iint_0^{k_0} \tilde{\boldsymbol{E}} \cdot \tilde{\boldsymbol{J}}^*\, dk_x\, dk_y\right\}, \tag{3}$$

where J is the electric current source density and E the E-field due to this current, both in the spatial Fourier domain. As a result, constructive interference occurs in the radiated field, leading to a maximum in radiated power while keeping a surface-wave suppression, as demonstrated in the next section.

III. Electric Current Ring Surface-Wave and Radiation

This section develops the analytical framework to extract the power radiated and coupled to SW of a ring of electric current. It is then demonstrated that, although the magnetic current has been replaced by an electric one compared to [35], SW suppression can be achieved following a different design rule.

A. Total Power

Considering a multilayer stack, as shown in Fig. 2(a), with a sheet antenna at any interface, the time-averaged active power that leaves this antenna can be expressed as:

$$P_{\text{out}} = \Re\left\{\frac{-1}{8\pi^2}\int_0^{2\pi}\int_0^{\infty} \tilde{\boldsymbol{E}} \cdot \tilde{\boldsymbol{J}}^*\, d\phi\, \beta\, d\beta\right\}, \tag{4}$$

with J the current density on the sheet and E the electric field due to this current. β and ϕ are respectively the transverse wave vector and the azimuthal angle in the Fourier domain, such that $k_x = \beta\cos(\phi)$, $k_y = \beta\sin(\phi)$. An equivalent expression is given in [39] in the spatial domain. The integration is performed in the Fourier domain such that the dyadic Green's function $\tilde{\boldsymbol{G}}$ can be expressed in closed form for a multilayer stack [40]. Equation (4) then becomes:

$$P_{\text{out}} = \Re\left\{\frac{-1}{8\pi^2}\int_0^{2\pi}\int_0^{\infty} \tilde{\boldsymbol{G}}\tilde{\boldsymbol{J}} \cdot \tilde{\boldsymbol{J}}^*\, d\phi\, \beta\, d\beta\right\}. \tag{5}$$

This study focuses on an electric current distribution following one period of a cosine along a ring of radius R, inspired by the magnetic current distribution from [35]. It can be expressed as:

$$\overline{\boldsymbol{J}}(\rho,\alpha) = \cos(\alpha)\delta(\rho - R)\hat{\boldsymbol{e}}_{\boldsymbol{\alpha}}, \tag{6}$$

with ρ and α being, respectively, the radial coordinate and the azimuthal angle in the spatial domain. A sketch of the current distribution J is shown in Fig. 2(b). Its Fourier transform, expressed in cylindrical coordinates, is given by:

$$\tilde{\boldsymbol{J}}(\beta,\phi) = \int_0^{2\pi}\int_0^{\infty} \overline{\boldsymbol{J}}(\rho,\alpha)e^{j\beta\rho\cos(\alpha-\phi)}\rho\, d\rho\, d\alpha. \tag{7}$$

Expressing the basis vector $\hat{e}_\alpha$ in Cartesian coordinates:

$$\hat{\boldsymbol{e}}_{\boldsymbol{\alpha}} = -\sin(\alpha)\hat{\boldsymbol{e}}_{\boldsymbol{x}} + \cos(\alpha)\hat{\boldsymbol{e}}_{\boldsymbol{y}}. \tag{8}$$

and using the Anger-Jacobi relation [41]:

$$\int_0^{2\pi}\begin{bmatrix}\sin(\alpha)\\ \cos(\alpha)\end{bmatrix} e^{j\beta\rho\cos(\alpha-\phi)}d\alpha = 2\pi j\begin{bmatrix}\sin(\phi)\\ \cos(\phi)\end{bmatrix} J_1(\beta\rho), \tag{9}$$

with $J_i(x)$ the ith Bessel function of the first kind, one finds the following expression for $\tilde{J}$:

$$\tilde{\boldsymbol{J}}(\beta,\phi) = J_2(\beta R)\sin(2\phi)\hat{\boldsymbol{e}}_{\boldsymbol{x}} + (J_0(\beta R) - J_2(\beta R)\cos(2\phi))\hat{\boldsymbol{e}}_{\boldsymbol{y}}. \tag{10}$$

For the reference stack considered in this paper, shown in Figs. 1(a) and (b), the Green's function can be expressed in the Fourier domain, following the same reasoning as in [40], as:

$$\tilde{\boldsymbol{G}} = \begin{bmatrix} \tilde{G}^{xx} & \tilde{G}^{xy} \\ \tilde{G}^{yx} & \tilde{G}^{yy} \end{bmatrix} = -\frac{1}{D_{\text{TE}}(\beta)} - \begin{bmatrix} \cos^2(\phi) & \cos(\phi)\sin(\phi) \\ \cos(\phi)\sin(\phi) & \sin^2(\phi) \end{bmatrix} \left(\frac{1}{D_{\text{TE}}(\beta)} - \frac{1}{D_{\text{TM}}(\beta)} \right), \tag{11}$$

where $D_{\text{TE}}(\beta)$ and $D_{\text{TM}}(\beta)$ are defined in [42]. When the antenna is at the uppermost interface, as in this case, they can be expressed as:

$$D_{\text{TE}}(\beta) = \frac{1}{k_0\eta_0}\left(k_{z,0} + k_{z,i}\frac{1-\Gamma_{\text{TE}}}{1+\Gamma_{\text{TE}}}\right) \tag{12}$$

$$D_{\text{TM}}(\beta) = \frac{k_0}{\eta_0}\left(\frac{1}{k_{z,0}} + \frac{\epsilon_{r,i}}{k_{z,i}}\frac{1+\Gamma_{\text{TM}}}{1-\Gamma_{\text{TM}}}\right). \tag{13}$$

k_0 and η_0 are respectively the free space wave vector and impedance of the air and i is the index of the layer underneath the interface where the antenna is located, Si or Quartz in the cases considered in this work. For a layer i, the z-oriented component of the wave vector is given by $k_{z,i} = \pm\sqrt{\epsilon_{r,i}k_0^2 - \beta^2}$, where the $+$ sign is chosen except for $k_{z,0}$ in the air, as discussed below. Γ_{TE} and Γ_{TM} are the reflection coefficients at the uppermost interface, looking downward, respectively computed from $\Gamma_{0,\text{TE}}$ and $\Gamma_{0,\text{TM}}$ [42], as defined in Fig. 2(a). The integral in (5) can be separated into two integration domains: the visible and the invisible regions.

B. Integration in the Visible Region: Radiation

In the lossless materials case, the contribution due to radiation into free space mathematically comes from the range of integration $k_x^2 + k_y^2 < k_0^2$ [39], that is the visible region. The physical meaning is that for each (k_x, k_y) pair in this region, $k_{z,0} = \sqrt{k_0^2 - \beta^2}$ is real, meaning that energy is leaving the structure towards the air region.

C. Integration in the Invisible Region: SW and Losses

The invisible region corresponds to the integration range $k_x^2 + k_y^2 > k_0^2$. The $k_{z,0}$ wavenumber component is therefore imaginary in this region. In the lossless materials case, the only contributor to the real part of the integral in the invisible region is the SW, that can diffract at the chip edges and distort the radiation pattern as introduced earlier. In the invisible region, the negative square root $k_{z,0} = -\sqrt{k_0^2 - \beta^2}$ should be selected to avoid field divergence as z tends towards $+\infty$.

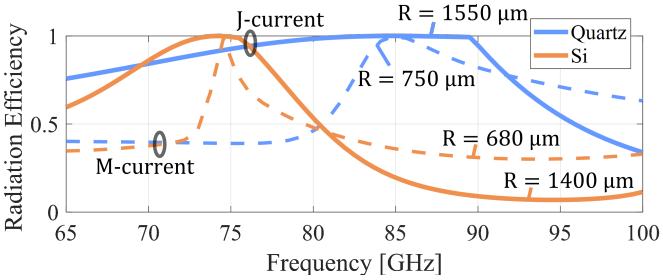


Fig. 3. Radiation efficiency of rings of magnetic and electric current in W-band for the reference Si and quartz stacks of Figs. 1(a) and (b) computed from (14).

D. Radiation Efficiency

The radiation efficiency e_r can be expressed in the lossless materials case as

$$e_r = \frac{P_{\text{Visible}}}{P_{\text{Visible}} + P_{\text{Invisible}}} \tag{14}$$

The radiated power corresponds to the integration of (5) in the visible region, denoted by P_{Visible}. The integration on the invisible region is denoted by $P_{\text{Invisible}}$. The same logic can be applied to magnetic current, separating the integration domain of (2) into visible and invisible regions and computing the Green's function from (11) using the duality principle [43]. Fig. 3 shows the radiation efficiency of rings of electric current J and magnetic current M in the lossless materials scenario on the reference chip and package stacks of Figs. 1(a) and (b). All antennas follow the current distribution of (6) and are designed to have a peak efficiency around 75 GHz on Si and 85 on Quartz. The ring radii are given on the figure in each case. It is demonstrated that, at the desired frequency, both M- and J-current distributions give rise to a zero in $P_{\text{Invisible}}$ and therefore theoretically yield a 100% radiation efficiency.

It can be noted that, as stated in the introduction, while the M-current distributions give rise to a peak at the desired frequencies, it is narrow-band compared to the J-current cases. This is due to the fact that, in the considered frequency range and on the reference stacks, the H-field of the wave reflected from the backplane conductor cancels out with the H-field of the wave radiating upward as stated in Section II, resulting in a low radiated power around the zero in $P_{\text{Invisible}}$. For the J-current, P_{Visible} assumes a peak in this frequency range while $P_{\text{Invisible}}$ goes through a zero, allowing a broader frequency band of high efficiency.

From Fig. 3, it is observed that, to obtain a peak in efficiency at a given frequency, a ring of electric current following the current distribution of (6) must have a different radius, as compared to a ring of magnetic current following the same distribution. The design rule for the case of a magnetic current has been derived by Jackson in [35], as reminded in (1). A new design rule must then be derived for the case of electric currents; that is the goal of the next section.

IV. New Design Rule For Electric Current

The method used in this paper to obtain the new design rule of a ring of electric current that does not excite SW differs from that used by Jackson in [35] for a magnetic current. It can although be shown that our approach allows to retrieve Jackson's design rule [see Appendix A].

In the lossless materials scenario, the only contributor to losses is the SW. It is possible to obtain an analytical expression of the power coupled to SW by extracting the residue of (5) as explained in [40] or [44]. The integral of (5) can be separated into two parts as

$$\int_0^\infty f(x)\,\mathrm{d}x = \mathrm{PV}\int_0^\infty f(x)\,\mathrm{d}x - j\pi\,\mathrm{Res}\{f(x)\}, \quad (15)$$

where PV stands for Cauchy's principal value, which only contributes to the radiated power, and *Res* for the residue of the integrand at the pole, that accounts for the power coupled to SW [40].

While combining the integral of (5) with the expression of the Green's function given in (11), the power coupled from any real valued current to the TM_0 SW mode can be shown to be equal, by calculating the residue using l'Hôpital's rule, to

$$\begin{aligned} P_{\mathrm{TM0}} = \Re\Bigg\{ & \frac{-j}{8\pi}\frac{N(\beta_{\mathrm{TM0}})}{D'(\beta_{\mathrm{TM0}})}\beta_{\mathrm{TM0}}\int_0^{2\pi}\Big[\cos^2(\phi)\left|\tilde{J}_x(\phi,\beta_{\mathrm{TM0}})\right|^2 \\ & + \sin^2(\phi)\left|\tilde{J}_y(\phi,\beta_{\mathrm{TM0}})\right|^2 \\ & + 2\cos(\phi)\sin(\phi)\tilde{J}_x(\phi,\beta_{\mathrm{TM0}})\tilde{J}_y(\phi,\beta_{\mathrm{TM0}})\Big]d\phi\Bigg\}. \end{aligned} \quad (16)$$

with β_{TM0} the propagation constant of the TM_0 SW mode and $1/D_{\mathrm{TM}}(\beta) = N(\beta)/D(\beta)$, with $D_{\mathrm{TM}}(\beta)$ given in (13). These quantities only depend on the stack parameters.

It is possible to cancel the ϕ integral in (16) to eliminate power coupling from an antenna to SW for a given material stack. For the current distribution given by (6), this leads to the following condition:

$$\begin{aligned} 0 = \int_0^{2\pi} & \Big[J_2^2(\beta_0 R)\sin^2(2\phi)\cos^2(\phi) \\ & + \big(J_0^2(\beta_0 R) + J_2^2(\beta_0 R)\cos^2(2\phi) \\ & - 2J_0(\beta_0 R)J_2(\beta_0 R)\cos(2\phi)\big)\sin^2(\phi) \\ & + 2\big(J_0(\beta_0 R)J_2(\beta_0 R)\sin(2\phi) \\ & - J_2^2(\beta_0 R)\sin(2\phi)\cos(2\phi)\big)\cos(\phi)\sin(\phi)\Big]d\phi. \end{aligned} \quad (17)$$

After evaluation of the trigonometric integrals, and using the property

$$J_2(x) + J_0(x) = \frac{2}{x}J_1(x), \quad (18)$$

one obtains the design rule for a ring of electric current:

$$J_1(\beta_{\mathrm{TM0}}R) = 0. \quad (19)$$

This yields,

$$\beta_{\mathrm{TM0}}R = 3.8317, \quad (20)$$

where the first root has been selected to maintain the design as compact as possible. Equation (20) is a fundamental design equation, which states that a ring of electric current will not excite the TM_0 SW, provided the radius R is chosen to satisfy it.

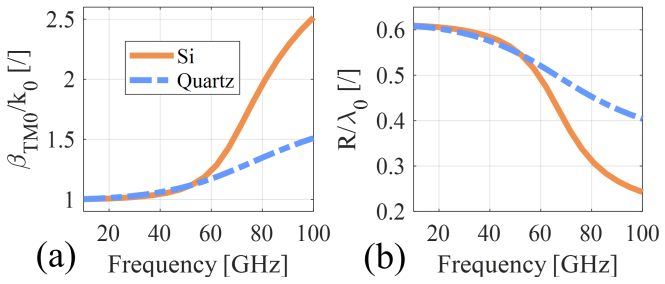


Fig. 4. (a) TM_0 SW propagation constant normalized by the free space wave vector in vacuum versus frequency. (b) Ring radius normalized by the free space wavelength versus frequency.

In Figs. 4(a) and (b) are shown respectively the TM_0 SW propagation constant normalized by the free space wave vector in vacuum and the ring radius normalized by the free space wavelength versus frequency. On both plots are considered the reference Si and quartz stacks of Figs. 1 (a) and (b). The electric ring radius has been evaluated using the new design rule (20) and the propagation constant of the fundamental SW mode has been obtained using the transverse resonance technique as described in [45]. This graph allows the estimate of the dimensions required by the antenna at each frequency for the two reference Si and Quartz stacks. As β_{TM0} moves from k_0, at low frequency, to k_{TEM} (i.e., the wavenumber of the transverse TEM mode in the substrate) at high frequency [45], the ratio R/λ_0 transitions from a constant value near 0.6 to another constant near 0.31 for quartz and 0.18 for Si.

It can be noticed that, although the design rule to avoid SW excitation of M- and J-current rings look similar, the M-current design rule involves the derivative of a Bessel function (1) while the new rule for J-current rings does not.

It can be mentioned that the design targets the dominant TM_0 surface-wave mode. The present design rule cancels only this SW mode. When higher-order modes become propagating and significantly excited, the single-root condition (20) is insufficient to suppress total substrate-mode power.The same methodology could be extended to higher-order modes using the same Green's-function framework, which is left for future work. It appears that rings of electric current should have a radius multiplied by a factor slightly larger than 2 to avoid SW excitation, compared to M-current. One could conclude that this will result in a larger area occupied by the antenna. In practice, as detailed in Section II, the magnetic current is implemented using a slot in a metal plane when no via is available. For the equivalence between magnetic current and slot to be valid, the dimensions of the metal plane should be sufficiently large compared to the wavelength, resulting in a large area occupied by the antenna. Furthermore, as described in Section III.D, for the reference stacks considered in this paper, the magnetic ring would suffer from strong destructive interference in the considered frequency band, leading to a very narrow peak in efficiency as shown in Fig. 3.

The next section discusses the implementation of such an antenna on both Si and Quartz substrates.

V. Electric Ring Implementation in W-Band on Si and Quartz Using One Metal Layer

This section presents the implementation of the novel RSW antenna concept using series capacitors to make the antenna with the desired ring radius resonant at the target frequency. Two prototypes are considered on the reference stacks shown in Figs. 1(a) and (b) as AoC and AiP demonstrators on Si and quartz substrates with respectively 80 and 85 GHz of central frequencies. The 500-µm quartz interposer considered here is used as a representative example; the proposed design rule is derived from the TM_0 propagation constant of the layer stack and therefore extends directly to other single- or multi-layer AiP substrates (e.g., thinner quartz/glass cores with polymer buildup layers).

A. Antenna Implementation with Series Capacitors

The electric ring is implemented using two in-phase curved dipoles in their first resonance mode. The current on a dipole at first resonance follows a cosine function on half a period with a maximum at its center and zeros at its edges imposed by the open-circuit boundaries. A dipole at first resonance has a length $\lambda_{\text{eff}}/2 = \lambda_0/(2\sqrt{\varepsilon_{r,\text{eff}}})$, where λ_0 is the free space wavelength in vacuum and $\varepsilon_{r,\text{eff}}$ is the effective relative permittivity, whose expression for a single grounded dielectric slab is given by [46]:

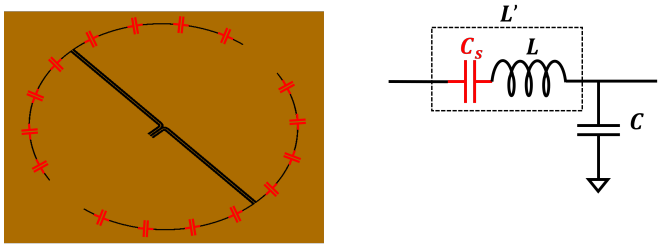
$$\varepsilon_{r,\text{eff}} = \frac{\varepsilon_r + 1}{2} + \frac{\varepsilon_r - 1}{2\sqrt{1 + \frac{10H}{W}}} \tag{21}$$

where H is the substrate thickness, W the dipole width and ε_r the relative permittivity of the material beneath the dipole. The values of H and ε_r are given on Figs. 1(a) and (b) for each substrate and the considered width is selected to be 10 µm.

The new design rule for a ring of electric current derived in Section IV imposes that, for a given frequency, the current should follow a period of a cosine function w.r.t. α on a circle of a certain radius R given by (20) to avoid SW excitation. At the design frequency, the two curved dipoles are not at first resonance as their length πR, with R imposed by (20), is greater than $\lambda_{\text{eff}}/2$. The first resonance frequency should therefore be shifted by increasing λ_{eff}.

To achieve this resonance frequency shift, series capacitors are periodically inserted into the dipole arms, as shown in Fig. 5(a). When neglecting radiation, the dipole arms can be modeled as lossless transmission lines made of cascaded blocks composed of a series inductance L and a shunt capacitance C, each block being small compared to the wavelength. This equivalent circuit is shown in Fig. 5(b). The L and C elements are linked to the effective wavelength by the effective propagation constant β_{eff}:

$$\beta_{\text{eff}} = 2\pi f\sqrt{LC} = \frac{2\pi}{\lambda_{\text{eff}}}. \tag{22}$$



(a) (b)

Fig. 5. (a) Scheme of the proposed implementation made of curved dipoles with series capacitors. (b) Transmission line equivalent circuit.

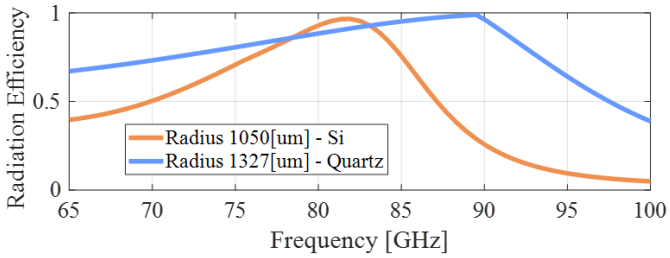


Fig. 6. Radiation efficiency of the considered antennas for the reference Si and quartz stacks of Figs. 1(a) and (b) computed from (14) in the lossless materials scenario.

The effective wavelength can be increased by reducing either L or C in each cascaded unit cell, which can be achieved by introducing a shunt inductance or a series capacitance. In this work, the former approach is adopted, as both on-chip and in-package technologies rely on fine lithography processes that enable the realization of high-density capacitors [47], [48]. Depending on the process, these capacitors may be implemented using parallel-plate or interdigitated topologies. The reduced equivalent inductance L' of each block can be expressed, considering the series capacitor C_s, as:

$$L' = L - \frac{1}{(2\pi f)^2 C_s}. \tag{23}$$

For the selected design frequency and substrate materials, the ring radii on silicon and quartz are chosen, referring to (20), as $R_{\text{Si}} = 1050\ \mu\text{m}$ and $R_{\text{quartz}} = 1327\ \mu\text{m}$, respectively, in order to avoid SW excitation. The corresponding radiation efficiencies, computed using (14) under lossless material assumptions, are shown in Fig. 6 for both geometries. To maintain a compact antenna footprint, a trade-off between ring radius and radiation efficiency was made in the silicon implementation. As a result, the operating frequency of the silicon-based antenna does not reach 100% efficiency, since it lies slightly above the cut-off frequency of the TE_1 mode. As shown in Fig. 6, only about 3% of the input power is coupled to SW, which is considered negligible. The cut-off frequency of the TE_1 SW mode can be shown to be around 75 and 90 GHz in the Si and Quartz cases [45].

From that result, eight series capacitors, uniformly spaced, are introduced on each curved dipole, as shown in Fig. 5(a). Their practical implementation and characterization is discussed in the next section.

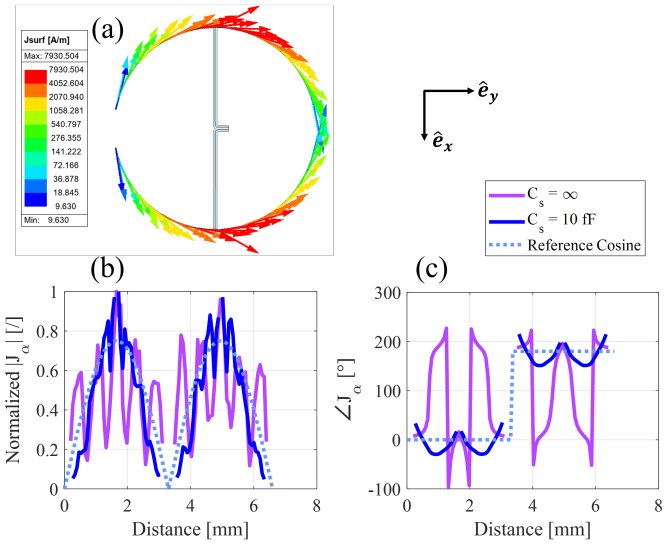


Fig. 7. (a) J_α vector on the ring on Si substrate. (b) Normalized magnitude and (c) phase of J_α on the ring for $C_s = \infty$ and $C_s = 10$ fF and a reference pure cosine function.

By extracting the phasor of the azimuthal current J_α along the ring in Ansys HFSS [49], it was found that, for a value of roughly 10 and 6 fF given to the series capacitor, on Si and quartz respectively, a current distribution close to a cosine is obtained. It is shown in Fig. 7 where both phase and normalized magnitude of J_α are plotted along with a pure cosine function as a reference for the two cases of the ring without series capacitor ($C_s = \infty$) and with the designed $C_s = 10$ fF series capacitors in the Si substrate case. It is demonstrated that the obtained current distribution is close to the ideal first resonance mode of the curved dipoles with the designed C_s. Several peaks and zeros are observed without series capacitor, corresponding to a higher-order resonance of the curved dipoles, which would be undesired. It should be mentioned that the obtained values of a few fF are well within the realm of practical implementation of industrial processes [48], [50]–[52] as it will be shown in the next section. In the simulations, the dipoles are fed from the center of the ring by a coplanar waveguide (CPW) line that splits into to in-phase coplanar strip (CPS) line, as shown in Fig. 5(a). On Fig. 7(b), the gaps correspond to intentional openings in the metal layout at the dipoles feeding point and at current-null locations to allow the routing of the feeding transmission line, as it will be discussed in Section VI-B.

B. Efficiency Analysis

The efficiency of the resulting ring antenna designs with 16 series capacitors has been extracted using a finite element method (FEM) in Ansys HFSS [49] and a MoM in ADS from Keysight [18], as shown in Fig. 8. Two loss scenarios have been considered for the quartz case: (i) lossless materials, (ii) lossy antenna and substrate (i.e., 2 kΩ·cm quartz, as characterized in the next section). For the Si case, in addition to the lossless scenario, three substrate resistivities are considered: (i) 3 kΩ·cm, representative of RF-grade high-resistivity substrates, (ii) 150 Ω·cm, and (iii) 20 Ω·cm, the

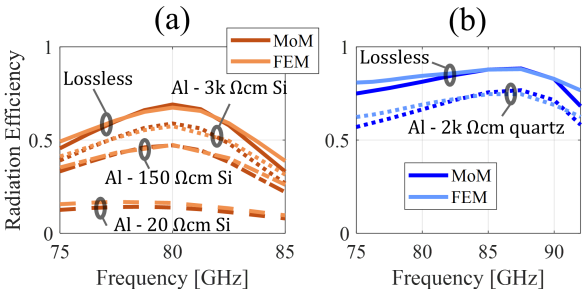


Fig. 8. Radiation efficiency obtained from full-wave simulations considering: (a) Four loss scenarios in the Si case. (b) Two loss scenarios in Quartz substrate.

latter two bracketing the typical medium- and low- resistivity values of standard commercial CMOS processes. In all lossy scenarios, the antenna is made of a 1-µm-thick aluminum layer ($\sigma_{\text{Al}} = 2.9 \times 10^7$ S/m). The 3 kΩ·cm scenario is the one experimentally investigated on Si in the next section. High correlation is obtained among the two solvers in each scenario. It is noted that for both solvers, in the lossless case, the efficiency reaches a peak near 70% on Si and 90% on quartz, meaning that at the peak, ∼30% of the power that leaves the antenna is in the form of a SW for the Si case and ∼10% for the quartz substrate. Neat uncoupling to SW is not reached as the current distribution obtained using series capacitors is not a pure cosine function as required by the design rule, but the distribution is close enough to this ideal case to reach a considerable SW coupling reduction.

While considering the lossy ring and substrate, the antennas reach a peak around 58% on high-resistivity (3 kΩ·cm) Si and 77% on quartz, meaning that ∼12 additional % of the power is lost through Joule's effect. In these two cases, the losses are dominated by the finite conductivity of the 1-µm aluminum antenna, while the substrate dielectric losses remain negligible. Performances could be improved by selecting higher conductivity metals such as Cu or Au. It can be mentioned that the capacitance values have been selected to enforce a cosine-like current distribution at the design frequency only, without any optimization for wideband operation. While an ideal cosine current at all frequencies is assumed in Fig. 6, full-wave simulations show a frequency-dependent current distribution, resulting in a slightly reduced operational bandwidth.

The propagation constant of the TM_0 surface-wave mode being negligibly affected by a reduction of the substrate resistivity [45], so is the electric-current design rule of Section IV, which depends only it. The intended current distribution can therefore be considered as independent on the substrate resistivity, even for standard low-resistivity substrate. However, unlike the high-resistivity case, conductive loss in the substrate is no longer negligible at lower resistivity and becomes the dominant loss mechanism. For the medium-resistivity 150 Ω·cm Si, an additional ∼10% efficiency drop is observed compared to the 3 kΩ·cm case, which can be considered acceptable given the lower cost of such substrates. For the low-resistivity 20 Ω·cm Si, representative of standard digital CMOS wafers, the efficiency drop is much more severe,

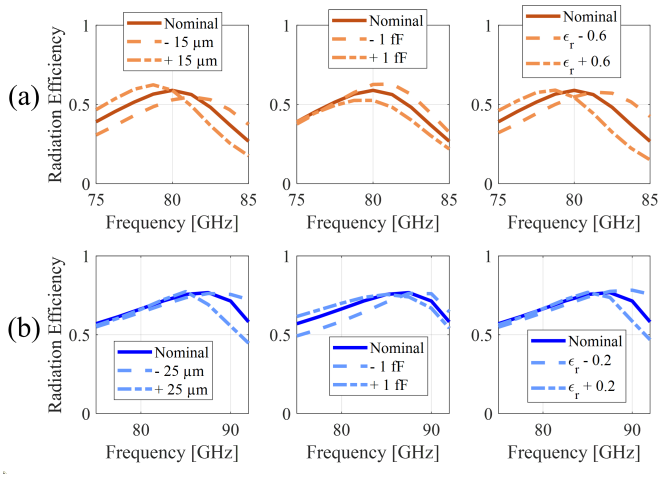


Fig. 9. Radiation efficiency sensitivity to fabrication tolerances on substrate thickness and series capacitance, for the lossy Si (a) and quartz (b) prototypes. Left: $\pm 15\,\mu$m (Si) and $\pm 25\,\mu$m (quartz) thickness variation, representative of typical wafer-thickness tolerances. Right: ± 1 fF capacitance variation.

reducing the peak efficiency to approximately 15%. This confirms that, while the proposed design rule remains valid even for low-resistivity substrate, the technique is best suited to high- and medium- resistivity silicon. Its use on low-resistivity digital-CMOS-grade substrates would require additional loss-mitigation measures to remain competitive.

Compared to the canonical dipoles on the same substrates, introduced in Fig. 1(c) that couple more than 80% of their power to SWs on Si and 40% on quartz, the SW efficiency, defined as the ratio of SW power to the sum of SW and radiated power, is reduced by more than a factor of 2.5 for both substrates, at the design frequency. Furthermore, the antennas occupy respectively an area smaller $\lambda_0^2/4$ on Si and $\lambda_0^2/2$ on quartz, making them a compact solution.

Contrary to ADS, which intrinsically does not account for SW in its extracted radiation efficiency, radiation boundary conditions must be imposed at lateral boundaries of the simulated space in HFSS, that capture the diffracted SW at the chip edges. A part of the SW power is therefore accounted for in the computed radiated power in these solvers. To avoid this ambiguity and to be able to distinguish the radiated power from the power coupled to SW, the chip has been enclosed within a buffer stack with the same dimensions and permittivity but with a 10 Ωcm substrate. In HFSS, the chips have lateral dimensions of 8 mm x 8 mm and are enclosed by buffer whose lateral dimensions are 20 mm x 20 mm. The buffer dimensions have been chosen such that at least 99% of the SW power that enters in it is dissipated before reaching the edge, while the attenuation constant of the SW has been computed using [45]. This approach relies on the assumption that all the SW power coming from the chip to the buffer is transferred in the buffer region. This is supposed to be true as the extracted propagation constant and characteristic impedance of the SW modes, extracted from a modal analysis in HFSS, are very close in the 'buffer' and in the 'chip' regions.

C. Tolerance Analysis

To assess the robustness of the proposed design against fabrication-induced variations, a parametric tolerance analysis has been performed on both prototypes, considering three sources of deviation: (i) variations in substrate thickness H, representative of typical wafer-thickness tolerances ($\pm 15\,\mu$m for Si, $\pm 25\,\mu$m for quartz, corresponding to $\pm 5\%$ of the nominal thickness for both substrates), (ii) variations in the series capacitor value C_s, consistent with the ± 1 fF variation observed between simulated and measured capacitance, as it will be discussed in Section VI-A and (iii) variation on the substrate permittivity ϵ_r of $\pm 5\%$ if both case. ADS simulations, following the same procedure as used for Fig. 8, have been repeated for each parameter varied independently about its nominal value, with the other parameter held fixed, for the lossy high-resistivity Si and quartz designs. The results are shown in Fig. 9(a) and (b) for the Si and quartz prototypes. In all cases, the radiation efficiency variation is lower than 5%, while a slight shift of the peak is observed, confirming that the design is reasonably robust to realistic process tolerances. Substrate-thickness and relative permittivity variations are observed to have the more pronounced effect of the three parameters: since the ring radius is fixed after fabrication, a change in H or ϵ_r alters the TM_0 mode propagation constant of which depends the design rule of (20), so the frequency at which SW suppression, and hence peak efficiency, occurs shifts accordingly. Capacitor-value variation has a comparatively smaller impact on the peak efficiency level, but similarly introduces a shift in the frequency at which the curved-dipole current distribution best approaches the ideal cosine shape required by (6), consistent with the role of C_s in tuning the effective propagation constant β_{eff} of (22). Overall, both prototypes retain their essential radiation-efficiency behavior over the considered fabrication tolerances, the operating band remaining centered near the nominal design frequency.

While this section has demonstrated how the ring of electric current can be implemented using series capacitors, these will be described and characterized in the next section.

VI. Characterization

A. Capacitance Design and Characterization Using One Metal Layer

In the previous section, it was shown that capacitance values of approximately 6 fF and 10 fF are required for the silicon and quartz antenna designs, respectively. This section describes how such capacitors are implemented using a single metal layer and subsequently characterized on both substrates.

Interdigitated capacitors are adopted, allowing to take advantage of the high resolution lithography (i.e. below 1 µm) offered by most processes nowadays while maintaining the design on one metal layer. Dedicated full-wave simulations of the capacitors were carried out to adjust their values where interdigitated capacitors with 1 µm spacing are considered. Considering the simplified equivalent circuit shown in Fig. 10(a), which models the structure as a two-port network

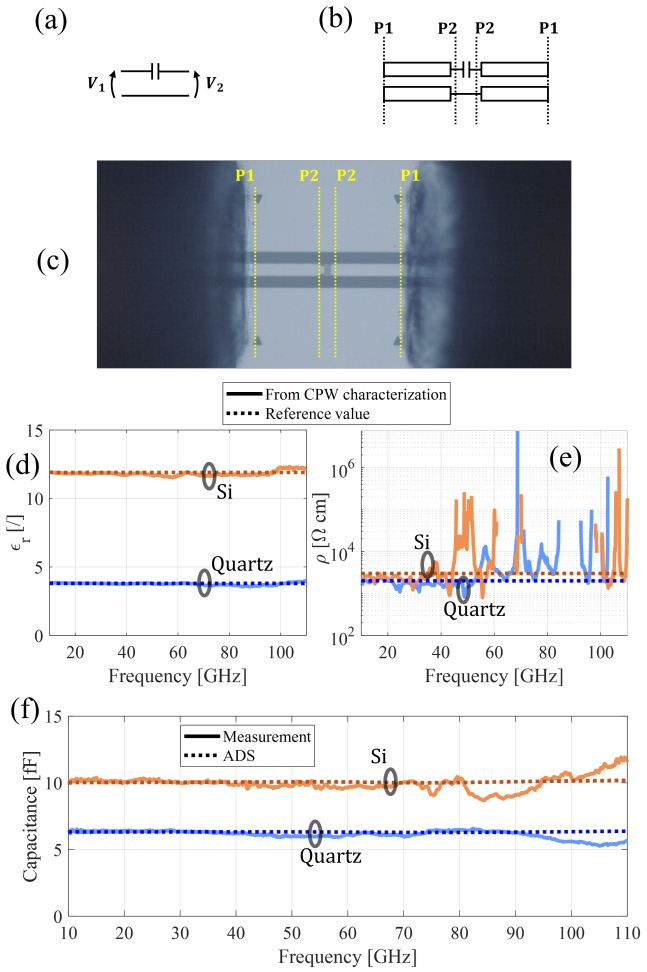


Fig. 10. (a) 2-ports network used to extract the capacitance value from the full-wave simulations. (b) Schematics of transmission line cascaded capacitance. (c) Microscope view of a capacitor connected through CPW access. (d) Substrates permittivity and (e) resistivity, extracted from CPW on-wafer characterization. (f) Simulated and measured capacitors values.

containing a series capacitance, the capacitance value is extracted from the simulated admittance matrix as

$$C = \frac{\Im\{Y_{11}\}}{2\pi f}. \tag{24}$$

To experimentally characterize the designed interdigitated capacitors, they were cascaded along the signal line of coplanar waveguide (CPW) structures, as illustrated in Figs. 10(b) and (c).

Figure 10(c) shows a microscope image of a CPW-cascaded capacitor. On-wafer S-parameter measurements were performed using an Agilent N5242A PNA-X vector network analyzer over the 10–110 GHz frequency range. A pair of GSG Infinity probes from FormFactor and an MPI probe station were employed. The reference planes at the probe tips (P1 in Figs. 10(b) and (c)) were established through a multiline TRL (mTRL) calibration, as described in [53], on a impedance standard substrate (ISS) . On the same wafers, standalone CPW lines (i.e. without integrated capacitors) of various lengths $\{280, 530, 1580, 2030, 3000, 5000\}$ µm and an open-circuit standard were fabricated, enabling the application of a second-tier on-wafer mTRL de-embedding to shift the reference planes at the edges of the capacitor (P2 in Figs. 10(b) and (c)) [54].

In addition to the shift of reference plane position, the second-tier mTRL de-embedding procedure applied to the CPW lines on-wafer enables the extraction of substrate parameters [55]. The extracted permittivity and resistivity values for both silicon and quartz substrates are reported in Figs. 10(d) and (e), respectively.

The extracted permittivity shows very good agreement with the reference values (i.e., $\varepsilon_r = 11.9$ for silicon and $\varepsilon_r = 3.8$ for quartz). Consequently, no frequency shift is expected for the antenna designs fabricated on the same wafers, which are presented in the next section.

Figure 10(e) further indicates that the extracted resistivity of both materials remains above 1 kΩcm over the entire characterized frequency band. Reference resistivity values of 3 kΩcm and 2 kΩcm are selected for the silicon and quartz substrates, respectively, and show good agreement with the extracted data at low frequencies.It should be noted that, for such low-loss substrates (i.e., $\rho \geq 1$ kΩcm), accurate resistivity extraction becomes increasingly challenging at higher frequencies, as conductor losses in the CPW dominate the overall attenuation and mask the relatively small contribution of substrate losses. Moreover, calibration inaccuracies introduce systematic errors that grow with frequency [55]. That explains the high fluctuation of the curves and missing portions, due to negative resistivity extraction. Overall, as mentioned, the extracted resistivity can be considered above 1 kΩcm over the frequency band, corresponding to an equivalent $\tan(\delta) < 5 \times 10^{-3}$ for both materials at 100 GHz.

Finally, Fig. 10(f) compares the simulated and measured capacitance values as a function of frequency. A good agreement is observed over most of the band, while slight deviations appear above 80 GHz, particularly for the silicon substrate. These discrepancies are attributed to calibration non-idealities or probe-dependent residual error inherent to on-wafer measurement at Sub-THz frequencies [56]. The observed variations, on the order of ±1 fF, remain acceptable for the proposed capacitively loaded antennas, as demonstrated in V-C, confirming the suitability of the designed capacitors.

The next section presents the mm-Wave antenna measurement results on silicon and quartz substrates.

B. mm-Wave Antenna Measurement

This section presents the implementation of the ring antennas on silicon and quartz substrates presented in Section V-A. The prototypes on Si and quartz are shown in Figs. 11(a) and (b) respectively. They have respective radii 1050 and 1327 µm as detailed previously. The antennas and their feeding networks are realized using a single metal layer and incorporate sixteen series interdigitated capacitors each, whose design and characterization are described in Section VI-A. A zoomed view on one capacitor is highlighted in each image of Fig. 11. The antennas are fed using CPW lines terminated with GSG pads, as shown in Fig. 11. At the center of the ring,

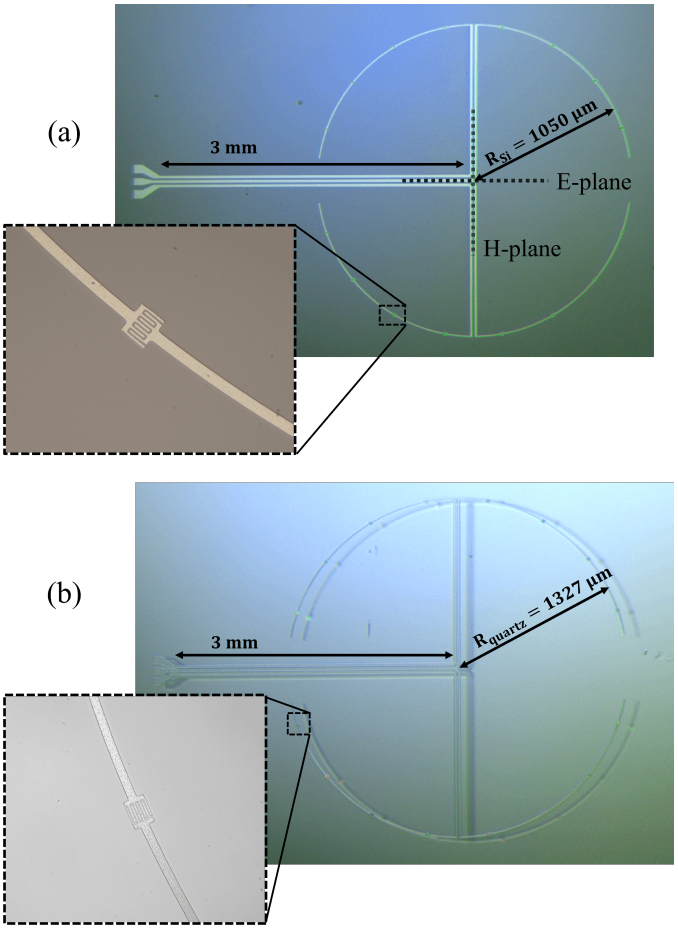


Fig. 11. Microscope view of the processed ring antennas with zoom on an interdigitated capacitor. (a) Si prototype. (b) Quartz prototype.

the same CPW to dual-CPS mode transition, as introduced in Section V-A for the efficiency simulations, is employed to excite both halves of the ring in phase. A 3-mm-long CPW access line is introduced to mitigate the influence of the bulky on-wafer probe on the radiated field during far-field measurements [58].

The antennas have been designed alongside the CPWs and capacitors described in Section VI-A on the same wafers. The structures were fabricated on bare 3-inch silicon and quartz wafers using a single-metal-layer process. A 1-µm-thick aluminum layer was deposited on both wafer sides by e-beam evaporation, with the backside metal serving as a continuous metal plane. The top layer was patterned using standard photolithography and chlorine-based plasma etching.

For the on-chip antenna measurements, the spherical antenna measurement system presented in [57] was employed. The on-wafer probe, as well as the overall measurement setup including the microscope and the reference horn antenna, are shown in Figs. 12(a) and (b), respectively. A Picoprobe Model 75 GSG probe was used and connected to a R&S ZNA43 VNA through a W-band frequency extender R&S ZC110. The realized gain of the antenna under test (AUT) is obtained by comparing the measured transmission coefficient S_{21} with that of a well-known horn antenna, while compensating for the losses introduced by the mm-Wave probe, following the procedure described in [60]. The gain is calculated as

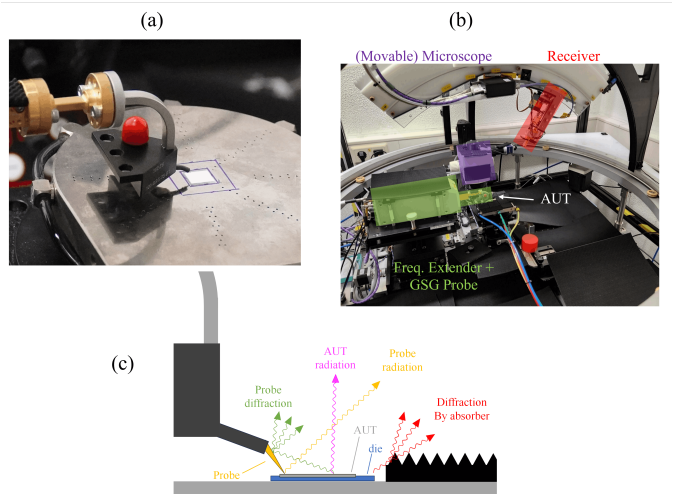


Fig. 12. (a) Close view of the on-wafer probe and metal chuck. (b) Full setup view. (c) Sketch of the effect of the absorber and the probe.

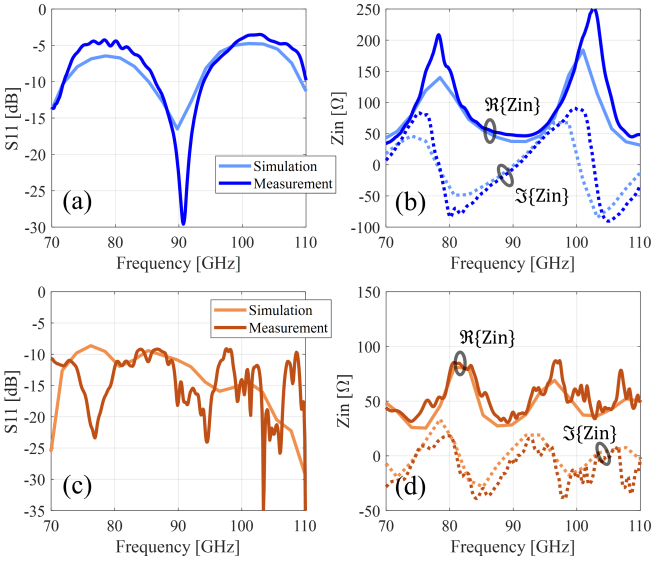


Fig. 13. Ring antennas S_{11} and Z_{in} versus frequency. Quartz prototype (a) and (b). Si prototype (c) and (d).

$$G_{\text{AUT}} = \frac{|S_{21,\text{AUT}}|^2}{|S_{21,\text{Probe}}|^2 |S_{21,\text{Horn}}|^2} G_{\text{Horn}}. \tag{25}$$

In (25), the probe losses are determined by extracting the error terms of the mm-Wave probe using on-wafer calibration open, short, and load standards. To minimize the impact of the measurement environment on the radiation pattern, most metallic parts of the setup, including the chuck, are covered with mm-Wave absorbers, as shown in Fig. 12(b). The parasitic effects associated with on-wafer far-field measurements are illustrated in Fig. 12(c). They include probe scattering and direct radiation, as well as scattering induced by the absorber [17].

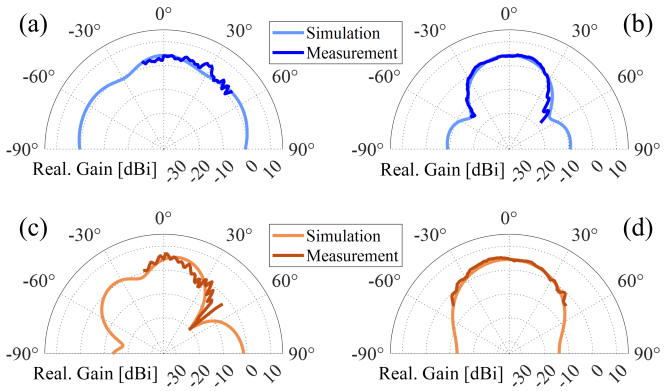


Fig. 14. Antennas realized gain measurement and simulation in co-polarization in two cut planes. Quartz prototype in (a) E-plane and (b) H-plane at 85 GHz. Si prototype in (c) E-plane and (d) H-plane at 80 GHz.

Fig. 13 presents the measured and simulated reflection coefficient (S_{11}) and input impedance (Z_{in}) of the silicon and quartz antennas. The reference plane is set at the probe tip using an SOL de-embedding procedure [59], while simulations are performed using Ansys HFSS. A good agreement between simulation and measurement is observed. Oscillations in the measured response are attributed to residual multipath effects, despite the use of mm-Wave absorbers [60]. No frequency shift is observed, in agreement with the permittivity characterization presented in Section VI-A. For the silicon antenna, the extremely low reflection coefficient level makes the measurement more sensitive to these oscillations, explaining the slightly reduced agreement observed in S_{11} compared to Z_{in} although the input impedance is extracted from the measured S_{11}.

Radiation pattern measurements are performed by rotating the receiver around the AUT in a spherical coordinate system. Two cut planes are measured in the E- and H-planes, as defined in Fig. 11. The H-plane is limited to $|\theta| \leq 50°$ to avoid collision with the microscope, while the E-plane spans $-15° \leq \theta \leq 50°$, as smaller angles are shadowed by the probe. The ring antenna exhibits a broadside main lobe with linear polarization along $\hat{\boldsymbol{e}}_{\boldsymbol{x}}$. This behavior is explained by the current distribution shown in Fig. 7: at broadside, the curved dipoles radiate in phase, resulting in cancellation of the $\hat{\boldsymbol{e}}_{\boldsymbol{y}}$-oriented field components and a net $\hat{\boldsymbol{e}}_{\boldsymbol{x}}$ polarization.

The realized gain in this polarization is shown in Fig. 14 for both cut planes at the center frequencies of 80 and 85 GHz for the silicon and quartz substrates, respectively. In both planes, a very good agreement between simulation and measurement is observed. In the E-plane, small oscillations are observed as well as a deviation around $\theta \approx 30°$. These are attributed to probe-induced reflections and scattering, as well as multipath within the measurement setup as observed in [34]. A broadside realized gain of approximately 5 dBi and 4 dBi is obtained for the silicon and quartz antennas, respectively.

Fig. 15 shows the realized broadside gain as a function of frequency. Once again, good agreement between simulation and measurement is obtained, while slight gain ripples are observed as previously discussed. The gain response is more stable over frequency for the quartz substrate, as expected due

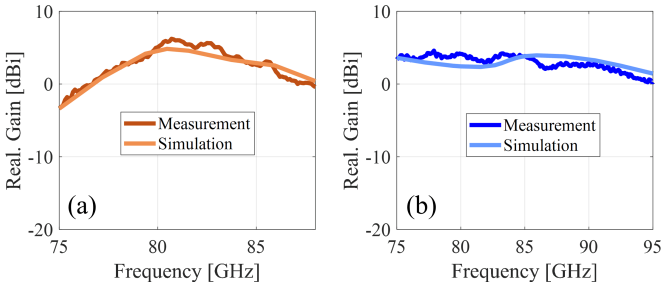


Fig. 15. Realized gain over frequeny. (a) Si prototype. (b) Quartz prototype.

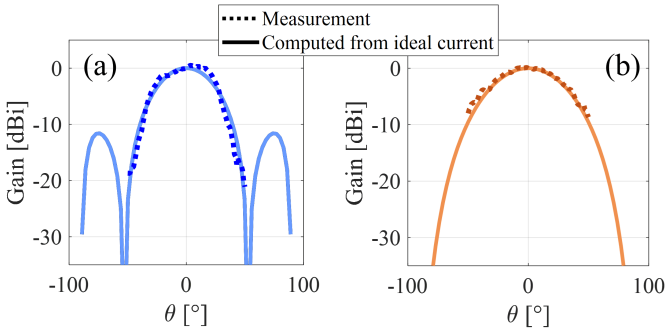


Fig. 16. Normalized measured radiation pattern in H-plane at 83 GHz compared with the theoretically predicted one assuming the ideal ring current distribution. Computed from (A10). (a) Quartz prototype. (b) Si prototype.

to its lower permittivity. The slightly higher gain of the silicon prototype compared to the quartz prototype is attributed to the residual impedance mismatch of the quartz antenna at the operating frequency.

Finally, to further assess the current distribution along the ring, the measured radiation pattern at 83 GHz is compared with the theoretically predicted pattern assuming an ideal lossless current distribution given by (6) on the reference substrate stacks. The comparison is shown in Fig. 16 as a function of the elevation angle θ. The radiated electric field and the corresponding normalized gain analytical computation are given in Appendix B. Only the H-plane radiation pattern is reported, since the E-plane measurements are significantly affected by probe shadowing and scattering effects, as discussed previously. These effects being not accounted for in the analytical model. A very good agreement is observed between the measured and theoretical patterns, demonstrating that the intended current distribution is effectively impressed along the ring through the use of the series capacitive loading.

C. Surface-Wave Coupling Characterization

This section provides experimental evidence of the reduction in SW coupling achieved by the proposed antenna. A coupling-based characterization approach is adopted for this purpose, following a technique used to quantify SW excitation at lower frequencies [63], [64]. In this approach, the transmission coefficient $\hat{S}_{21}$ between the AUT and a fixed reference probe antenna, both placed on the same substrate, is measured and used as an indicator of the SW power coupled into the substrate.

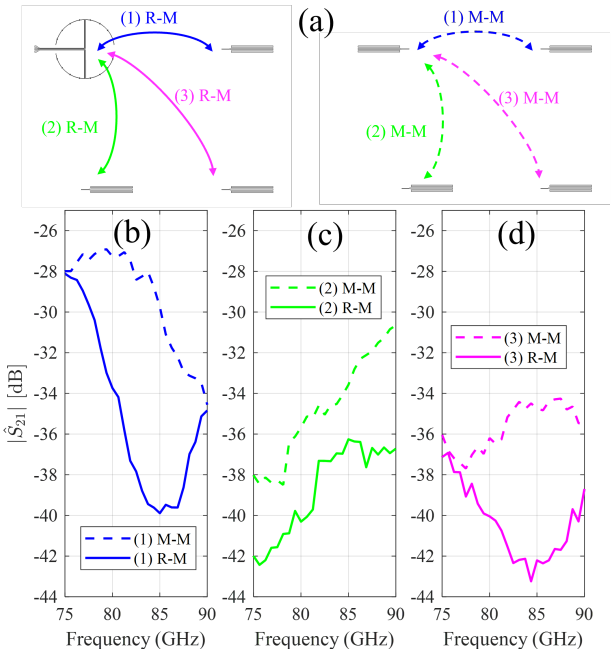


Fig. 17. (a) configuration sketch. (b)–(d) Two-port SW coupling measurement results for the three configurations, for the ring-monopole and monopole-monopole cases.

Because the considered process allows only a single metal layer and no through-substrate vias, a single-ended quarter-wavelength monopole is used as a probe instead of the coaxial pins used in [63], [64]. The monopole is fed directly from a CPW line, consistent with the feeding approach used for the ring antenna itself and compatible with on-wafer probing. The monopole is used both as the reference antenna, for a monopole-monopole (M-M) coupling baseline, and as the coupling probe for the ring-monopole (R-M) characterization.

The measurement procedure is as follows: after an ISS-based on-wafer calibration, identical to that described in Section VI-A, the coupling is measured between (i) the proposed ring antenna and a reference monopole, and (ii) two reference monopoles, referred to respectively as the R-M and M-M configurations. For both cases, three relative positions of the receiving probe are considered, as illustrated in Fig. 17(a): (1) at 2 cm from the ring center along the axis of the feed-line extension, (2) at 2 cm along the orthogonal grid axis, and (3) at 2 cm along each of the two grid axes simultaneously, corresponding to a diagonal (45°) direction at a center-to-center distance of $2\sqrt{2} \approx 2.83$ cm. The separation distance of 2 cm ($\approx 5.5\lambda_0$ at 83 GHz) was selected to keep the free-space coupling contribution small relative to the substrate-mediated coupling within that constraint. The structures were fabricated for this measurement on the high-resistivity silicon substrate described in Fig. 1(a). The measurement was performed using the same probes and calibration procedure described in Section VI-A.

To enable a fair comparison between the R-M and M-M configurations and to remove the influence of impedance mismatch, the normalized coupling factor introduced in [63] is used:

$$|\hat{S}_{21}| = \frac{|S_{21}|}{\sqrt{(1-|S_{11}|^2)(1-|S_{22}|^2)}}. \tag{26}$$

Fig. 17(b)–(d) show the measured $|\hat{S}_{21}|$ for the R-M and M-M configurations, for the three relative positions defined above.

As expected from the directional TM_0 coupling of a linear antenna at first resonance such as the monopole [65], the M-M coupling is strongest in configuration (1), along the probe axis [Fig. 17(b)]. The R-M coupling is also strongest in this same configuration, consistent with the ring antenna's own current distribution: since the ring is composed of two curved dipoles fed along a common axis, its residual (non-ideal) TM_0 excitation is expected to be strongest along that same feed-line axis. In this direction, the R-M coupling is nonetheless reduced by 6.5 dB relative to the M-M baseline at the design frequency of 80 GHz, with a minimum observed around 85 GHz where a reduction of more than 10 dB is observed compared to the M-M case. Solving the design rule (20) for the fabricated ring radius R_{Si} = 1050 µm yields a predicted TM_0-suppression frequency of 84 GHz, in close agreement with the coupling minimum observed in Fig. 17(a). This agreement provides direct quantitative support for the underlying design-rule mechanism.

For configuration (2) [Fig. 17(c)], corresponding to the direction along which the TE_1 mode is expected to couple most strongly for a linear antenna at first resonance [65], the coupling is increasing with frequency above its cut-off at 75 GHz [Section V-A], while being weaker compared to case (1). This is consistent with the TE_1 mode being only weakly excited by the ring over at the design frequency of 80 GHz, as explained in Section V-A, and a very little portion of the input power is expected to couple to this mode near this frequency. The R-M coupling in this configuration is nonetheless reduced relative to the M-M baseline across the band, consistent with the weaker overall SW coupling of the ring design.

Finally, in the diagonal configuration (3) [Fig. 17(d)], intermediate between the TM_0- and TE_1-dominant directions, a minimum in the R-M coupling is again observed near the predicted TM_0-suppression frequency. The relative reduction is however smaller than in configuration (1), as expected since this direction corresponds to neither the maximum of the TM_0 nor of the TE_1 SW pattern.

Taken together, these measurements provide experimental evidence consistent with the analytically predicted reduction of SW in Section V-A and observed indirectly through the pattern and input impedance agreement of Section VI-B.

D. Comparison with State-of-the-Art

Table I compares the proposed antennas with previously reported mm-Wave AoC and AiP designs that address SW excitation or radiation efficiency without relying on through-substrate vias, auxiliary radiating elements (e.g., dielectric resonators, lenses, superstrates), or additional processing steps. Solutions relying on artificial magnetic conductors (AMC) or metasurfaces [31], [62] achieve competitive efficiency and gain, but require two or three metal layers to implement

TABLE I
COMPARISON OF THE PROPOSED ANTENNA WITH PREVIOUSLY REPORTED ON-CHIP AND IN-PACKAGE ANTENNAS AT MM-WAVE FREQUENCIES, WITHOUT THROUGH-SUBSTRATE VIAS, ADDITIONAL RADIATORS, OR COMPLEXIFIED PROCESSES.

Ref.	Freq. (GHz)	Technology	Solution to avoid SW	Metal layers	Area (λ_0^2)	3-dB BW (%)	Peak meas. Gain (dBi)	Peak Eff. (%)
[12]	135	LTCC	Thin substrate	2	1.00	4.4	11.0	–
[61]	140	40-nm CMOS	Edge radiation	1	0.07	15	-2.7	–
[62]	94	In-house CMOS-compatible process	Substrate shielding with AMC	2	1.57	5.9	9.8	72[a]
[31]	139	28-nm bulk CMOS	Dipole array with AMC	3	0.20	19	2.3	30[b]
[15]	120	130-nm SiGe	Dipole array, dual SW-mode cancellation	2	0.15	8	-2.5	–
[This work]	80	In-house lithography on Si	Tailored current	1	0.25	10	4.9	58[a]
	85	In-house lithography on Quartz	Tailored current	1	0.50	20	4.2	77[a]

[a] Simulated.
[b] Measured.

the shielding or feeding structure. The dipole-array SW-cancellation approach of [15], conceptually the closest prior work to the present design, achieves a compact footprint ($0.15\,\lambda_0^2$) using two metal layers, but does not report a radiation or surface-wave efficiency figure, and its cancellation is inherently partial, as discussed in Section I. Edge-radiating and thin-substrate approaches [12], [61] avoid surface-wave excitation altogether by geometry rather than by current shaping, at the expense of either low gain or a non-negligible thickness constraint.

In contrast, the proposed antennas are, to the best of our knowledge, the only reported solution combining explicit surface-wave reduction with single-metal-layer, vialess compatibility, while reaching peak simulated efficiencies of 58% on Si and 77% on quartz within a compact footprint of 0.25–$0.5\,\lambda_0^2$. We further note that surface-wave efficiency is not reported for several of the compared designs [12], [15], [61], which limits a fully quantitative efficiency comparison across the table; nonetheless, the combination of measured gain, compact area, and single-layer compatibility indicates that the proposed approach offers a favorable trade-off in terms of process complexity and antenna performances among the solutions considered.

VII. CONCLUSION

This paper has introduced a new millimeter-wave planar antenna concept which excites little surface-wave power. The proposed approach relies on an electric current distribution implemented using series capacitors loading, enabling surface-wave mitigation using a single metal layer without additional fabrication steps, auxiliary radiating elements, or multilayer metallization, making it compatible with both AoC and AiP technologies. The design is based on the principle, introduced in this paper for the first time, that a ring of electric current in a multilayer grounded stack does not excite the dominant TM_0 surface wave when its radius is properly selected. From the Green's function analysis in the Fourier domain, the design rule for such a ring is derived as a tool for antenna designers. Two W-band prototypes fabricated on silicon and quartz substrates are presented as AoC and AiP demonstrators. A strong reduction of surface-wave excitation on electrically thick substrates is demonstrated as the surface-wave efficiency, defined as the ratio of surface-wave power to the sum of radiated and surface-wave power, is reduced by more than a factor of 2.5 compared with a conventional half-wavelength dipole on the same substrate stack. This confirms the effectiveness of the proposed electric-current-based approach for surface-wave control across substrates with different permittivities.

The prototypes were characterized through full-wave simulations and on-wafer measurements, demonstrating good agreement. Far-field measurements validated the radiation behavior, with broadside radiation and realized gains of approximately 5 dBi on silicon and 4 dBi on quartz. Furthermore, a reduction of substrate coupling is experimentally demonstrated by 2-ports measurements on-wafer. The proposed antennas remain compact, occupying areas smaller than $\lambda_0^2/4$ on silicon and $\lambda_0^2/2$ on quartz.

It should be mentioned that the proposed approach has several limitations. First, the analytical design rule targets the dominant TM_0 surface-wave mode; higher-order modes are not explicitly canceled and may become relevant for thicker substrates or higher frequencies. Second, exact cancellation assumes a continuous cosine current distribution, whereas the practical implementation using discrete series capacitors realizes this distribution only approximately. Third, the cancellation condition depends on the TM_0 propagation constant and therefore is intrinsically dependent on the substrate stack and operating frequency. Finally, the achievable total efficiency remains sensitive to substrate conductivity and metal loss, as illustrated by the significant efficiency reduction obtained for low-resistivity silicon.

The presented antenna concept provides an effective, compact, and fabrication-friendly solution for single metal layer mm-wave AoC and AiP applications, competitive with state of the art solutions in terms of performances.

APPENDIX

A. Jackson's Design Rule Derived with Our Method

Considering a magnetic current distribution following a cosine along a ring of radius R, as given in [35], it can be expressed as

$$\bar{\boldsymbol{M}}(\rho,\alpha) = \cos(\alpha)\delta(\rho - R)\hat{\boldsymbol{e}}_{\boldsymbol{\alpha}}, \tag{A1}$$

with ρ and α being, respectively, the radial coordinate and the azimuthal angle in the spatial domain.

From (5) and using the duality principle, the power coupled from any real-valued magnetic current to the TM_0 SW mode can be shown to be proportional to a certain integral, using l'Hôpital's rule, as

$$\begin{aligned} P_{\mathrm{TM0}} \propto \int_0^{2\pi} \Big(& \sin^2(\phi)|\tilde{J}_x(\phi,\beta_{\mathrm{TM0}})|^2 \\ & + \cos^2(\phi)|\tilde{J}_y(\phi,\beta_{\mathrm{TM0}})|^2 \\ & - 2\cos(\phi)\sin(\phi)\tilde{J}_x(\phi,\beta_{\mathrm{TM0}})\tilde{J}_y(\phi,\beta_{\mathrm{TM0}}) \Big) d\phi, \end{aligned} \tag{A2}$$

with β_{TM0} the propagation constant of the TM_0 SW mode.

To cancel the power coupled from a magnetic current source to the SW for a given material stack, it is possible to cancel the ϕ integral in (A2). For the magnetic current distribution of (A1), this leads to the following condition:

$$\begin{aligned} 0 = \int_0^{2\pi} \Bigg(& J_2^2(\beta_0 R)\sin^2(2\phi)\sin^2(\phi) \\ & + \Big(J_0^2(\beta_0 R) + J_2^2(\beta_0 R)\cos^2(2\phi) \\ & - 2J_0(\beta_0 R)J_2(\beta_0 R)\cos(2\phi) \Big)\cos^2(\phi) \\ & - 2\Big(J_0(\beta_0 R)J_2(\beta_0 R)\sin(2\phi) \\ & + J_2^2(\beta_0 R)\sin(2\phi)\cos(2\phi) \Big) \\ & \times \cos(\phi)\sin(\phi) \Bigg) d\phi. \end{aligned} \tag{A3}$$

After evaluation of the trigonometric integrals, and using the identity

$$J_2(x) - J_0(x) = -2J_1'(x), \tag{A4}$$

one obtains the design rule for a ring of electric current:

$$J_1'(\beta_{\mathrm{TM0}}R) = 0, \tag{A5}$$

which is the same as given in [35].

B. Theoretical Gain of Ring Antenna in H-plane

The considered electrical current distribution in the Fourier domain, given in (10). By computing its projection on $\hat{\boldsymbol{\phi}}$ basis vector as

$$\hat{\boldsymbol{\phi}} = -\sin(\phi)\hat{\boldsymbol{e}}_{\boldsymbol{x}} + \cos(\phi)\hat{\boldsymbol{e}}_{\boldsymbol{x}}, \tag{A6}$$

one obtains

$$\tilde{J}_\phi = \hat{\boldsymbol{\phi}} \cdot \tilde{\boldsymbol{J}} = -2\pi\rho_0\, J_1'(\beta R)\cos\phi. \tag{A7}$$

All the quantities have been defined in Section III-A.
By combining this expression with the spectral Green's function of (11), one can show that the far field expression of the radiated $\vec{E}$ oriented along $\hat{\boldsymbol{\phi}}$ in the H-plane is given by

$$E_{\mathrm{FF},\phi}(\theta,\phi,r) = -\frac{j}{2\pi}\, k_z\, \frac{\tilde{J}_\phi(\phi)}{D_{\mathrm{TE}}}\, \frac{e^{-jk_0 r}}{r}, \tag{A8}$$

with k_0 the free space wave vector of the air, k_z its vertical component, r the distance to the observer and θ the elevation angle. D_{TE} expression is given in (12). A similar expression can be found in [39] for the case of a dipole antenna.
The gain in this polarization can finally be computed as

$$G_\phi = 4\pi r^2 \frac{|E_{\mathrm{FF},\phi}|^2}{2\eta_0 P_{\mathrm{out}}}, \tag{A10}$$

where the expression of P_{out} is given in (5) while η_0 is the free space impedance in vacuum.

REFERENCES

[1] T. Jaeschke, C. Bredendiek, and N. Pohl, "A 240 GHz ultra-wideband FMCW radar system with on-chip antennas for high resolution radar imaging," IEEE MTT-S Int. Microw. Symp., Seattle, USA, Jun. 2013, pp. 1–4. DOI: 10.1109/MWSYM.2013.6697495

[2] G. P. Kniffin and L. M. Zurk, "Model-based material parameter estimation for terahertz reflection spectroscopy," IEEE Trans. Terahertz Sci. Technol., vol. 2, no. 2, pp. 231–241, Mar. 2012. DOI: 10.1109/TTHZ.2011.2181921

[3] K. K. Tokgoz, et al., "A 120 Gb/s 16 QAM CMOS millimeter-wave wireless transceiver," IEEE Int. Solid-State Circuits Conf. (ISSCC), San Francisco, USA, Feb. 2018, pp. 168–170.

[4] S. Li, et al., "Performance of V-band on-chip antennas in globalfoundries 45 nm CMOS SOI process for mm-wave 5G applications," IEEE MTT-S Int. Microw. Symp., Philadelphia, USA, pp. 1593-1596, Jun. 2018.

[5] Y. Yang, O. D. Gurbuz, and G. M. Rebeiz, "An eight-element 370–410-GHz phased-array transmitter in 45-nm CMOS SOI with peak EIRP of 8–8.5 dBm," IEEE Trans. Microw. Theory Tech., vol. 64, no. 12, pp. 4241–4249, Dec. 2016. DOI: 10.1109/TMTT.2016.2613850

[6] R. Malmqvist, et al., "A W-band single-chip receiver in a 60 nm GaN-on-silicon foundry process," 16th European Microwave Integrated Circuits Conference (EuMIC), London, United Kingdom, 2022. DOI: 10.23919/EuMIC50153.2022.9784092

[7] S.-Y. Tang, J. Chen, X. Xia, P. Zhou, H. Lu, L. Chang, et al., "Terahertz on-chip aperture antenna with through substrate vias for enhanced gain and chip-size insensitivity in InP technology," IEEE Trans. Antenn. Propag., vol. 71, no. 9, pp. 7184–7195, Sep. 2023. DOI: 10.1109/TAP.2023.3292502

[8] Y. Dong, T. K. Johansen, and V. Zhurbenko, "On-chip patch antenna on InP substrate for short-range wireless communication at 140 GHz," SBMO/IEEE MTT-S International Microwave and Optoelectronics Conference (IMOC), Aguas de Lindoia, Brazil, 2017. DOI: 10.1109/IMOC.2017.8121032

[9] M. Frank et al., "Antenna and package design for 61- and 122-GHz radar sensors in embedded wafer-level ball grid array technology," IEEE Trans. Microw. Theory Tech., vol. 66, no. 12, pp. 5156-5168, Dec. 2018, doi: 10.1109/TMTT.2018.2873368

[10] T. Galler, T. Frey, C. Waldschmidt, and T. Chaloun, "High-gain millimeter-wave holographic antenna in package using glass technology," IEEE Antennas Wirel. Propag. Lett., vol. 19, no. 12, pp. 2067–2071, Dec. 2020. DOI: 10.1109/LAWP.2020.3022520

[11] T. Frey, M. Döring, C. Waldschmidt, and T. Chaloun, "A full tensorial synthesis method for holographic-based leaky-wave antennas," IEEE Antennas Wirel. Propag. Lett., vol. 23, no. 2, pp. 553–557, Feb. 2024. DOI: 10.1109/LAWP.2023.3329586

[12] A. A. Farid, A. S. H. Ahmed, A. Dhananjay and M. J. W. Rodwell, "A fully packaged 135-GHz multiuser MIMO transmitter array tile for wireless communications," in IEEE Transactions on Microwave Theory and Techniques, vol. 70, no. 7, pp. 3396-3405, July 2022, doi: 10.1109/TMTT.2022.3161972.

[13] N. G. Alexopoulos, P. B. Katehi, and D. B. Rutledge, "Substrate optimization for integrated circuit antennas," IEEE Trans. Microw. Theory Tech., vol. MTT-31, no. 7, pp. 550–557, Jul. 1983. DOI: 10.1109/TMTT.1983.1131544

[14] L. Delait, C. Craeye, J. -P. Raskin and D. Lederer, "Analytical expressions for antenna on-chip efficiency at mm-Wave and Sub-THz frequencies," 2025 55th European Microwave Conference (EuMC), Utrecht, Netherlands, 2025, pp. 930-933, doi: 10.23919/EuMC65286.2025.11235230

[15] V. Lammert, M. Leyrer, M. Hamouda, R. Weigel, and V. Issakov, "Dual mode substrate wave cancellation in a 120 GHz 2 × 2 on-chip dipole array," IEEE Trans. Antenn. Propag., vol. 70, no. 8, pp. 6683–6691, Aug. 2022. DOI: 10.1109/TAP.2022.3161330

[16] A. Babakhani, X. Guan, A. Komijani, A. Natarajan, and A. Hajimiri, "A 77-GHz phased-array transceiver with on-chip antennas in silicon: Receiver and antennas," IEEE J. Solid-State Circuits, vol. 41, no. 12, pp. 2795–2806, Dec. 2006. DOI: 10.1109/JSSC.2006.884811

[17] L. Delait, et al., "Planar leaky-wave antenna design on thick substrate by radiating surface waves using strip rings," 49th International Conference on Infrared, Millimeter, and Terahertz Waves (IRMMW-THz), Perth, Australia, pp. 1-2, 2024. DOI: 10.1109/IRMMW-THz60956.2024.10697743

[18] Advanced Design System (ADS), Keysight Technologies, Santa Rosa, USA. [Online]. Available: https://www.keysight.com/us/en/products/software/pathwave-design-software/pathwave-advanced-design-system.html

[19] S. D. Lee et al., "Wideband, High Efficiency On-Chip Monolithic Integrated Antenna at W-Band Using Miniaturized Cavity and Through Silicon Via," IEEE Trans. Compon. Packag. Manuf. Technol., vol. 14, no. 12, pp. 2355-2363, 2024, doi: 10.1109/TCPMT.2024.3495520

[20] C. -W. Chiang, C. -T. M. Wu, N. -C. Liu, C. -J. Liang and Y. -C. Kuan, "A Cost-Effective W-Band Antenna-in-Package Using IPD and PCB Technologies," in IEEE Transactions on Components, Packaging and Manufacturing Technology, vol. 12, no. 5, pp. 822-827, May 2022, doi: 10.1109/TCPMT.2022.3170499

[21] W. T. Khan, A. Cagri Ulusoy, G. Dufour, M. Kaynak, B. Tillack, J. D. Cressler, et al., "A D-band micromachined end-fire antenna in 130-nm SiGe BiCMOS technology," IEEE Trans. Antenn. Propag., vol. 63, no. 6, pp. 2449–2459, 2015. DOI: 10.1109/TAP.2015.2416751

[22] W. H. Syed, G. Fiorentino, D. Cavallo, M. Spirito, P. M. Sarro, and A. Neto, "Design, fabrication, and measurements of a 0.3 THz on chip double slot antenna enhanced by artificial dielectrics," IEEE Trans. Terahertz Sci. Technol., vol. 5, no. 2, pp. 288–298, Mar. 2015. DOI: 10.1109/TTHZ.2015.2399276

[23] D. Hou, J. Chen, P. Yan and W. Hong, "A 270 GHz × 9 Multiplier Chain MMIC With On-Chip Dielectric-Resonator Antenna," in IEEE Transactions on Terahertz Science and Technology, vol. 8, no. 2, pp. 224-230, March 2018, doi: 10.1109/TTHZ.2017.2786027.

[24] D. F. Filipovic, S. S. Gearhart, and G. M. Rebeiz, "Double-slot antennas on extended hemispherical and elliptical silicon dielectric lenses," IEEE Trans. Microw. Theory Tech., vol. 41, no. 10, pp. 1738–1749, Oct. 1993. DOI: 10.1109/22.247919

[25] K. Lin, K. Guo, H. Guo, K. Man Shum, K. Fai Chan, and C. Hou Chan, "A 180–194-GHz power amplifier co-designed with a power-combining end-fed slot antenna array in 65-nm CMOS," IEEE Trans. Microw. Theory Tech., vol. 73, no. 2, pp. 965–976, Feb. 2025. DOI: 10.1109/TMTT.2024.3441942

[26] G. Guimaraes and P. Reynaert, "A 670-GHz 4 × 2 oscillator–radiator array achieving 7.4-dBm EIRP in 40-nm CMOS," IEEE J. Solid-State Circuits, vol. 56, no. 11, pp. 3399–3411, Nov. 2021. DOI: 10.1109/JSSC.2021.3093365

[27] P. Gan et al., "Full W-Band HDI Antenna-in-Package Array Based on a Coplanar Magnetoelectric Dipole," in IEEE Antennas and Wireless Propagation Letters, vol. 25, no. 6, pp. 2416-2420, June 2026, doi: 10.1109/LAWP.2026.3681000.

[28] H. S. Bakshi et al., "180-GHz Broadside Radiation Bond-Wire Antenna for Short-Range Wireless Communication," IEEE Trans. Compon. Packag. Manuf. Technol., vol. 11, no. 3, pp. 530-532, 2021, doi: 10.1109/TCPMT.2021.3053558.

[29] N. Llombart, A. Neto, G. Gerini, and P. de Maagt, "Planar circularly symmetric EBG structures for reducing surface waves in printed antennas," IEEE Trans. Antenn. Propag., vol. 53, no. 10, pp. 3210–3218, Oct. 2005. DOI: 10.1109/TAP.2005.856365

[30] M. H. Nemati and I. Tekin, "A 77GHz on-chip microstrip patch antenna with suppressed surface wave using EBG substrate," 2013 IEEE Antennas and Propagation Society International Symposium (APSURSI), Orlando, USA, pp. 1824-1825, 2013. DOI: 10.1109/APS.2013.6711571

[31] S. Sinha, M. Libois, K. Vaesen, H. Suys, L. Pauwels, and I. Ocket, "Miniaturized (127 to 154) GHz dipole arrays in 28 nm bulk CMOS with enhanced efficiency," IEEE Trans. Antenn. Propag., vol. 69, no. 3, pp. 1414–1426, Mar. 2021. DOI: 10.1109/TAP.2020.3031411

[32] X. Sun et al., "RF Si interposer platform for chiplets based heterogenous systems," 2025 IEEE 75th Electronic Components and Technology Conference (ECTC), Dallas, TX, USA, 2025, pp. 189-196, doi: 10.1109/ECTC51687.2025.00038

[33] V. Lammert, M. Hamouda, R. Weigel, and V. Issakov, "A 122 GHz on-chip 3-element patch antenna array with 10 GHz bandwidth," 50th European Microwave Conference (EuMC), Utrecht, Netherlands, pp. 599-602, 2021. DOI: 10.23919/EuMC48046.2021.9337954

[34] B. Sievert, J. Wittemeier, J. T. Svejda, N. Pohl, D. Erni and A. Rennings, "Bandwidth-enhanced circularly polarized mm-wave antenna with on-chip ground plane," IEEE Trans. Antenn. Propag., vol. 70, no. 10, pp. 9139-9148, Oct. 2022, doi: 10.1109/TAP.2022.3184539

[35] D. R. Jackson, J. T. Williams, A. K. Bhattacharyya, R. L. Smith, S. J. Buchheit, and S. A. Long, "Microstrip patch designs that do not excite surface waves," IEEE Trans. Antenn. Propag., vol. 41, no. 8, pp. 1026–1037, Aug. 1993. DOI: 10.1109/8.244643

[36] D. R. Jackson, "Reduced surface wave microstrip antennas," Handbook of Antenna Technologies, by eds. Chen Z.N. 1933-1968, Springer, 2016. DOI: 10.1007/978-981-4560-44-3_50

[37] M. A. Hickey, M. Qiu, and G. V. Eleftheriades, "A reduced surface-wave twin arc-slot antenna for millimeter-wave applications," IEEE Microw. Wirel. Compon. Lett., vol. 11, no. 11, pp. 459–461, Nov. 2001. DOI: 10.1109/7260.966041

[38] S. A. Adekola and K. A. Amusa, "Impact of ground plane size on fields radiated by slot antennas," IEEE 3rd International Conference on Electro-Technology for National Development (NIGERCON), Owerri, Nigeria, 2017. DOI: 10.1109/NIGERCON.2017.8281878

[39] P. Perlmutter, S. Shtrikman, and D. Treves, "Electric surface current model for the analysis of microstrip antennas with application to rectangular elements," IEEE Trans. Antenn. Propag., vol. 33, no. 3, pp. 301–311, Mar. 1985. DOI: 10.1109/TAP.1985.1143581

[40] J. R. Mosig, "Integral equation technique," in Numerical Techniques for Microwave and Millimeter-Wave Passive Structures, T. Itoh, Ed. New York: Wiley, 1989, pp. 133–213.

[41] M. Abramowitz and I. Stegun, Handbook of Mathematical Functions with Formulas, Graphs, and Mathematical Tables, Washington, DC, US Government Printing Office, 1964.

[42] J. Cavillot, "Fast electromagnetic analysis of large objects involving planar layered media : application to antenna arrays and metasurfaces", Ph.D. dissertation, Louvain-la-Neuve: Université catholique de Louvain, Belgium, 2021.

[43] R. F. Harrington, Time-Harmonic Electromagnetic Fields. New York: McGraw-Hill, 1981, pp. 98–100.

[44] N. Uzunoglu, N. Alexopoulos, and J. Fikioris, "Radiation properties of microstrip dipoles," IEEE Trans. Antenn. Propag., vol. 27, no. 6, pp. 853–858, Nov. 1979. DOI: 10.1109/TAP.1979.1142173

[45] L. Delait, et al., "Silicon resistivity impact on surface waves for antenna on-chip applications," IEEE Asia-Pacific Microwave Conference (APMC), Bali, Indonesia, pp. 635-637, 2024. DOI: 10.1109/APMC60911.2024.10867596

[46] M. V. Schneider, "Microstrip lines for microwave integrated circuits," Bell Syst. Tech. J., vol. 48, no. 5, pp. 1421–1444, May-Jun. 1969. DOI: 10.1002/j.1538-7305.1969.tb04274.x

[47] J. Shi, et al., "Evolution and optimization of BEOL MOM capacitors across advanced CMOS nodes," 48th European Solid-State Device Research Conference (ESSDERC), Dresden, Germany, pp. 190-193, 2018. DOI: 10.1109/ESSDERC.2018.8486905

[48] C. Roda Neve et al., "High-density and low-leakage novel embedded 3D MIM capacitor on Si interposer," 2016 IEEE International 3D Systems Integration Conference (3DIC), San Francisco, CA, USA, 2016, pp. 1-4, doi: 10.1109/3DIC.2016.7970024.

[49] H. F. S. S. Ansys, Ansys Inc., Canonsburg, USA. [Online]. Available: https://www.ansys.com/products/electronics/ansys-hfss

[50] M. Rack, et al., "A compact 120 GHz LNA in 22 nm FD-SOI with back-gate controllable variable-gain," 18th European Microwave Integrated Circuits Conference (EuMIC), Berlin, Germany, pp. 386-389, 2023. DOI: 10.23919/EuMIC58042.2023.10288898

[51] I. Kim, W. Kim, and S. Hong, "A D-band variable-gain LNA with triple-inductive coupling gm-boosting," IEEE Int. Sympos. on Radio-Freq. Integr. Techn. Busan, Korea: RFIT, 2022, pp. 194–196.

[52] P. J. Artz, et al., "A fully-differential 146.6-157.4 GHz LNA utilizing back gate control to adjust gain in 22 nm FDSOI,"

IEEE/MTTS Int. Microw. Symp., Denver, USA, pp. 611-614, 2022. DOI: 10.1109/IMS37962.2022.9865523
[53] R. B. Marks, "A multiline method of network analyzer calibration," IEEE Trans. Microw. Theory Tech., vol. 39, no. 7, pp. 1205-1215, July 1991, doi: 10.1109/22.85388
[54] S. Liu et al., "New methods for series-resistor calibrations on substrates with losses up to 110 GHz," IEEE Trans. Microw. Theory Tech., vol. 64, no. 12, pp. 4287-4297, Dec. 2016, doi: 10.1109/TMTT.2016.2609911.
[55] Nyssens L, Rack M, Raskin J-P., "Effective resistivity extraction of low-loss silicon substrates at millimeter-wave frequencies," Int. J. Microw. Wirel. Technol., vol. 12, 2020., doi:10.1017/S175907872000077X
[56] L. Nyssens, "A systemic analysis of silicon substrates toward improvements of integrated FD-SOI circuits performance at mm-wave frequencies", pp. 134-143, Ph.D. dissertation, Louvain-la-Neuve: Université catholique de Louvain, Belgium, 2023.
[57] B. Sievert, J. T. Svejda, D. Erni and A. Rennings, "Spherical mm-Wave/THz antenna measurement system," IEEE Access, vol. 8, pp. 89680-89691, 2020, doi: 10.1109/ACCESS.2020.2993698
[58] L. Boehm, M. Hitzler, F. Roos and C. Waldschmidt, "Probe influence on integrated antenna measurements at frequencies above 100 GHz," 2016 46th European Microwave Conference (EuMC), London, UK, 2016, pp. 552-555, doi: 10.1109/EuMC.2016.7824402.
[59] L. F. Tiemeijer, R. J. Havens, A. B. M. Jansman and Y. Bouttement, "Comparison of the "pad-open-short" and "open-short-load" deembedding techniques for accurate on-wafer RF characterization of high-quality passives," IEEE Trans. Microw. Theory Tech., vol. 53, no. 2, pp. 723-729, Feb. 2005, doi: 10.1109/TMTT.2004.840621.
[60] S. Beer and T. Zwick, "Probe based radiation pattern measurements for highly integrated millimeter-wave antennas," Proc. 4th Eur. Conf. Antennas Propag., Barcelona, Spain, pp. 1–5, Apr. 2010.
[61] Y. Qian, Y. Shen, Y. Ding, H. Cai, K. Zhang and S. Hu, "A D-Band Highly Integrated Low-Noise I/Q Receiver With On-Chip Antenna and Lossy Embedding Network in 40-nm CMOS," in IEEE Transactions on Microwave Theory and Techniques, vol. 73, no. 11, pp. 8868-8878, Nov. 2025, doi: 10.1109/TMTT.2025.3583087.
[62] Y. Yu, Z. Akhter, and A. Shamim, "Improving the performance of antenna-on-chip by effectively illuminating the artificial magnetic conductors through coupling enhancement structures," IEEE Trans. Antenn. Propag., vol. 71, no. 5, pp. 4492–4497, May 2023. DOI: 10.1109/TAP.2023.3239102
[63] G. Amendola, L. Boccia and G. Di Massa, "Shorted elliptical patch antennas with reduced surface waves on two frequency bands," IEEE Trans. Antenn. Propag., vol. 53, no. 6, pp. 1946-1956, June 2005, doi: 10.1109/TAP.2005.848469.
[64] Meide Qiu and G. V. Eleftheriades, "Highly efficient unidirectional twin arc-slot antennas on electrically thin substrates," IEEE Trans. Antenn. Propag., vol. 52, no. 1, pp. 53-58, Jan. 2004, doi: 10.1109/TAP.2003.822412.
[65] Rogers, R.L., Neikirk, D.P. "Use of broadside twin element antennas to increase efficiency on electrically thick dielectric substrates," Int. J. Infrared Milli Waves 9, 949–969, 1988. https://doi.org/10.1007/BF01010768

AUTHOR'S BIOS TO BE ADDED